







**First-order magnetic phase transition in Pr<sub>2</sub>In with negligible thermomagnetic hysteresis**Anis Biswas <sup>1,\*</sup>, N. A. Zarkevich <sup>1</sup>, Arjun K. Pathak <sup>1,2</sup>, O. Dolotko,<sup>1</sup> Ihor Z. Hlova,<sup>1</sup> A. V. Smirnov,<sup>1</sup> Y. Mudryk <sup>1</sup>, D. D. Johnson <sup>1,3</sup> and V. K. Pecharsky <sup>1,3</sup><sup>1</sup>*Ames Laboratory, U.S. Department of Energy, Iowa State University, Ames, Iowa 50011, USA*<sup>2</sup>*Department of Physics, SUNY Buffalo State, Buffalo, New York 14222, USA*<sup>3</sup>*Department of Materials Science and Engineering, Iowa State University, Ames, Iowa 50011, USA*

(Received 2 March 2020; accepted 11 May 2020; published 1 June 2020)

Magnetic first-order phase transitions are key for the emergence of functionalities of fundamental and applied significance, including magnetic shape memory as well as magnetostrictive and magnetocaloric effects. Such transitions are usually associated with thermomagnetic hysteresis. We report the observation of a first-order transition in Pr<sub>2</sub>In from a paramagnetic to a ferromagnetic state at  $T_C = 57$  K without a detectable thermomagnetic hysteresis, which is also accompanied by a large magnetocaloric effect. The peculiar electronic structure of Pr<sub>2</sub>In exhibiting a large density of states near the Fermi energy explains the highly responsive magnetic behavior of the material. The magnetic properties of Pr<sub>2</sub>In are reported, including observation of another (second-order) magnetic transition at 35 K.

DOI: [10.1103/PhysRevB.101.224402](https://doi.org/10.1103/PhysRevB.101.224402)**I. INTRODUCTION**

Discontinuous first-order magnetic phase transitions (FOMPTs) are less common than their continuous, second-order equivalents. Exhibited by a broad variety of materials and systems that range from ionic solids to metals, semimetals, and semiconductors, FOMPTs are a vibrant area of research because their occurrence may lead to useful functionalities, such as giant magnetocaloric effect, giant magnetostriction, and colossal magnetoresistance [1–18]. These phenomena often arise when magnetic (dis)order-order transitions occur in parallel with changes in the underlying crystal lattice, leading to magnetostructural transformations (MSTs), which are commonly associated with thermomagnetic hysteresis [1–13]. Cycling a material across a hysteretic MST results in energy losses [1] which are detrimental to energy conversion applications, solid-state caloric cooling being one example. Over the years, considerable research efforts have been dedicated to designing materials with MSTs where concurrent changes of magnetic and crystallographic sublattices occur with the smallest possible hysteresis [1–12].

Recent studies reveal that the hysteresis can be manipulated and reduced, enhancing the functionality of materials exhibiting MSTs, for example, improving reversibility of the giant magnetocaloric effect [12–18]. So far, materials where hysteresis could be successfully minimized are nearly exclusively transition-metal-based [5,18–21]. In these cases, crystallographic symmetry commonly remains unperturbed across the corresponding FOMPTs, despite discontinuous changes in phase volume prescribed by thermodynamics. One well-known example is the family of LaFe<sub>13–x</sub>Si<sub>x</sub>-based materials exhibiting a giant magnetocaloric effect with narrow hysteresis, tunable between ~200 and 350 K by chemical

substitutions and/or hydrogenation [14,15]. Magneto-volume changes in this and similar materials are also known as magnetoelastic transformations (METs), and they are commonly related to a peculiar nature of itinerant-electron metamagnetism (IEM) [14,15].

In lanthanide-based materials, the 4*f* electronic states are highly localized, and indirect magnetic exchange occurs through Ruderman–Kittel–Kasuya–Yosida (RKKY)-type interactions [22,23] where 5*d* electrons of the lanthanides play a vital role in the indirect exchange [24,25]. The long-range magnetic order of trivalent lanthanide ions is therefore strongly dependent on the 4*f*–5*d* hybridization and is generally supported by itinerant *s*, *p*, and *d* electrons. The enhancements of these itinerant electronic states often come from constituent elements other than the lanthanides themselves [8]. Assuming close association between IEM and magnetoelastic behaviors, it is believed that classical METs should be rather uncommon in RKKY-type systems, such as magnetic lanthanide-based intermetallic compounds [8]. However, the distinction between MSTs and METs is not always clear or meaningful, because magnetoelastic phenomena may or may not involve the changes of global symmetry and chemical bonding, while MSTs can be second order as well [26,27]. Furthermore, the isosymmetric nature of a transformation does not necessarily indicate a lack of hysteresis. For example, a ferromagnetic (FM)-antiferromagnetic (AFM) transition in Gd<sub>5</sub>Ge<sub>4</sub> is magnetoelastic, but it can be kinetically arrested at low temperatures and occurs with rather broad hysteresis, all without changing the crystallographic symmetry [28]. Therefore, the basic science of MET/MSTs, and the factors determining the hysteretic/anhysteretic behaviors associated with FOMPTs, remain an interesting and debated topic in materials physics.

Recently, an FOMPT between high-temperature paramagnetic (PM) and low-temperature FM states accompanied by a giant magnetocaloric effect with negligibly small

\*Corresponding author: [anis@ameslab.gov](mailto:anis@ameslab.gov)

thermomagnetic hysteresis was reported in a rare-earth-based intermetallic compound  $\text{Eu}_2\text{In}$  [8]. Even though  $\text{Eu}_2\text{In}$  is expected to be a typical RKKY-type exchange system and its chemical makeup is free of transition elements, magnetoelastic behaviors of this compound are strikingly similar to those of typical IEM transition-metal systems with FOMPTs. For example, the crystallographic symmetry of orthorhombic  $\text{Eu}_2\text{In}$  remains unperturbed across the transition. In rare-earth-based compounds with no transition elements, the magnetic order is nearly exclusively supported by indirect  $4f-4f$  coupling of lanthanide ions mediated by  $4f-5d$  exchange and  $5d-5d$  interactions between neighboring rare-earth ions [24,25,29]. However, the scenario observed in  $\text{Eu}_2\text{In}$  is more complicated. The Eu is purely divalent ( $4f^7 5d^0$ ), hence, filling of the Eu  $5d$  states occurs as a result of hybridization with In  $5p$  states, which leads to the development of large exchange splitting and emergence of long-range FM order [8].

The discovery of anhysteretic FOMPT and a giant magnetocaloric effect in  $\text{Eu}_2\text{In}$  leads to the interesting fundamental question of whether discontinuous magnetic and/or structural transformations may exist in other  $\text{R}_2\text{In}$  compounds, where R is rare-earth. Considering the difference in crystal structure types—at room temperature  $\text{Eu}_2\text{In}$  and  $\text{Yb}_2\text{In}$  adopt orthorhombic  $\text{Co}_2\text{Si}$  type, while the rest of the  $\text{R}_2\text{In}$  compounds crystallize in the hexagonal  $\text{Ni}_2\text{In}$  type [8]—one would expect to observe different behaviors in orthorhombic and hexagonal binary  $\text{R}_2\text{In}$ . Yet, an earlier study by Forker *et al.* indicates a discontinuous change in the magnetic hyperfine field in  $\text{Pr}_2\text{In}$  and  $\text{Nd}_2\text{In}$  compounds, likely pointing to first-order magnetic transitions in these hexagonal materials [29]. However, basic knowledge about the thermodynamic nature of the magnetic transition, the magnetic ground state, electronic structure, and hysteresis of  $\text{Pr}_2\text{In}$  is lacking. Further, it remains unknown how these materials respond when external thermodynamic variables, such as the magnetic field and hydrostatic pressure, vary near the phase transition.

Here, we conclusively verify the occurrence of an FOMPT in  $\text{Pr}_2\text{In}$ . We experimentally demonstrate that, similar to  $\text{Eu}_2\text{In}$ , the transition in  $\text{Pr}_2\text{In}$  is anhysteretic, despite dissimilar room-temperature crystal structures and regardless of potentially different mechanisms that support magnetic ordering, as the electronic configuration of  $\text{Pr}^{3+}$  ( $4f^2 5d^1$ ) is different from that of  $\text{Eu}^{2+}$  ( $4f^7 5d^0$ ). The FOMPT in  $\text{Pr}_2\text{In}$  expectedly results in a large magnetocaloric effect (MCE). Experimental findings are rationalized with first-principles electronic-structure calculations that reveal electronic instability near the Fermi energy ( $E_F$ ), manifested through a much-enhanced density of states (DOS) at  $E_F$ , which triggers the discontinuous phase transition in  $\text{Pr}_2\text{In}$ .

## II. EXPERIMENTAL METHODS

### A. Sample preparation

Two  $\text{Pr}_2\text{In}$  samples were prepared using different methods to verify the reproducibility of physical properties and whether the properties are dependent on the preparation and processing history. The first sample, henceforth sample 1, was synthesized by arc-melting of stoichiometric amounts of constituent elements in a Zr-gettered Ar atmosphere. The In

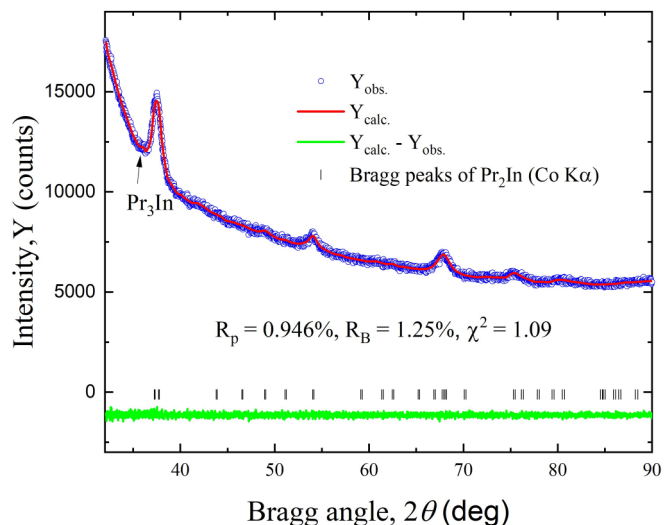


FIG. 1. Fully refined powder x-ray diffraction pattern of  $\text{Pr}_2\text{In}$  (sample 1).

was purchased from Alfa-Aesar, USA (Puratronic, 99.995 wt% pure), and Pr was supplied by the Materials Preparation Center of Ames Laboratory, USA (99.95 wt% pure with respect to all other elements in the periodic table). The alloy weighing 3 g was remelted five times, flipping the button upside down after each melting to ensure chemical homogeneity. After melting, the as-solidified material was annealed at 700 °C for three weeks in a quartz tube sealed under  $\sim 0.3$  bar of pure He and subsequently cooled slowly after the furnace was turned off. The formation of hexagonal  $\text{Pr}_2\text{In}$  and phase purity were confirmed with powder x-ray diffraction (see Fig. 1 and discussion below).

The second sample, hereafter sample 2, was prepared using the same starting elements taken in a stoichiometric ratio in a tantalum crucible. After loading the metals (4 g total), the crucible was sealed inside a quartz ampoule under  $\sim 0.3$  bar of pure He and placed inside a resistance furnace at room temperature. Synthesis was achieved by ramping the temperature up to 1470 K (approximately 100 K above the liquidus temperature [30]), holding for 5 h, then furnace-cooling to 1290 K (the temperature at which the peritectic reaction  $\text{L} + \text{Pr}_6\text{In}_5$  occurs [30]) at a rate of 30 K/h, and then kept there for 24 h. Afterward, the material was slowly cooled to 1220 K (just above the next peritectic reaction temperature  $\text{L} + \text{Pr}_2\text{In} = \text{Pr}_3\text{In}$  [30]) at a rate of 1.6 K/h and then quenched into the ice-water mixture. The prepared sample consisted of small and shiny crystallites visible to the eye. The main phase was hexagonal  $\text{Pr}_2\text{In}$  (over 95 vol %), the remainder representing cubic  $\text{Pr}_3\text{In}$  impurity, both determined using powder x-ray diffraction.

Regardless of the preparation method, both  $\text{Pr}_2\text{In}$  samples are exceedingly air sensitive, and they decompose in less than an hour when exposed to the atmosphere (standard laboratory air-conditioned air with 40%–50% humidity). Therefore, sample handling was performed in a glovebox (MBraun) with Ar used as cover gas. The main difference between these two polycrystalline materials is the grain size, as formation of large crystallites is expected in a slowly cooled sample. Quantitative characterization of grain-size differences with

either optical or electron microscopy unfortunately proved impossible due to the high reactivity of the prepared materials.

### B. Powder x-ray diffraction

Room-temperature powder x-ray diffraction (PXRD) examination was performed using the PANalytical X'Pert Pro powder diffractometer utilizing Co  $K\alpha$  radiation. Considering that the samples, especially in powder form, are strongly air sensitive, the powders were prepared and mounted on a sample holder inside a glovebox and then covered with a thin Kapton film to protect the powders from reaction with air during the measurements. The presence of the Kapton film visibly enhances the background in the PXRD patterns, especially at low Bragg angles. The full-profile Rietveld refinement of PXRD data was performed using FULLPROF [31] to extract crystallographic parameters and quantify the phase contents in both samples.

### C. Magnetic measurements and magnetocaloric effect

DC magnetization measurements were performed in a superconducting quantum interference device (SQUID) magnetometer, magnetic property measurement system (MPMS), manufactured by Quantum Design, Inc. Magnetic transition temperatures were determined from the temperature dependencies of isofield magnetization,  $M(T)$ , measured in a 1 kOe magnetic field ( $H$ ) during both heating and cooling. The temperatures corresponding to the fastest changes in  $M(T)$ , determined as the minima of the temperature derivatives,  $\partial M(T)/\partial T$ , were taken as Curie temperatures,  $T_C$ . The four-quadrant isothermal  $M(H)$  loops were recorded at 5 K in the magnetic field ranging between  $-50$  and  $+50$  kOe after cooling the samples in zero field from 300 K. Pressure-dependent  $M(T)$  data (at 2 kOe magnetic field) were also collected in the same magnetometer employing a Cu-Be cell manufactured by HMD (type CC-SPr-8.5D-MC4), with lead added as an internal manometer together with the sample, and Daphne (7373) oil used as a pressure-transmitting medium. The magnitude of applied hydrostatic pressure was determined from the superconducting transition temperature of lead measured by AC magnetic susceptibility on cooling, as described earlier [8]. The magnetic-field-induced entropy change ( $\Delta S_M$ ), one of the important parameters quantifying the magnetocaloric effect (MCE), was computed from  $M(T)$  data measured in different magnetic fields using Maxwell's equation. We employed  $M(T)$  data measured using the field-cooled warming (FCW) protocols, i.e., when the sample was first cooled to 5 K in the presence of different applied magnetic fields, then isofield magnetization was measured upon warming in the same fields, to avoid spurious errors [32,33].

### D. Specific heat

Specific heat,  $C_p$ , measurements were performed between 1.8 and 100 K in magnetic fields up to 20 kOe employing the relaxation method using a physical property measurement system, PPMS, manufactured by Quantum Design, Inc. The temperature dependence of entropy at zero magnetic field is calculated as  $S(T, H = 0) = \int_{T_i}^{T_f} \frac{C_p(T, H=0)}{T} dT$ , where  $T_i = 1.8$  K and  $T_f \leq 100$  K. The magnitude of a steplike

change in  $S(T, H = 0)$  at  $T_C$  is the measure of the total entropy change associated with the transition ( $\delta S_T$ ). However, we note that, in contrast to the magnetic measurements, the heat-capacity sample was briefly exposed to air during transfer from the glovebox to the PPMS. Due to strong sensitivity to air and, potentially, to traces of moisture that could be present in the Apiezon N grease used for the sample mounting, we expect that a minor surface decomposition could be present in the sample used to measure specific heat. Therefore the heat-capacity results reported in this work are semiquantitative.

## III. COMPUTATIONAL METHODS

Spin-polarized, density-functional-theory (DFT) calculations of  $\text{Pr}_2\text{In}$  were performed employing two codes, namely, the all-electron Korringa-Kohn-Rostoker (KKR) [34,35] Green's function (MECCA) code [36,37], and the full-potential Vienna *Ab-initio* Simulation Package (VASP) pseudopotential code [38,39]. The electronic (spin-decomposed) DOS was computed using MECCA [36] within the generalized gradient approximation (GGA) exchange-correlation energy functional for solids (PBEsol) [40]. Deep-core electrons were treated as fully relativistic using a Dirac solver (including In  $4s$  and  $4p$  and Pr  $4s$ ,  $4p$ ), while all other electrons at higher energies, including valence electrons closer to the Fermi energy  $E_F$ , were treated in a scalar-relativistic approximation (i.e., no spin orbit coupling). The electronic structure was calculated using KKR with the atomic sphere approximation (ASA) with periodic boundary corrections to account for interstitial electron contributions to Coulomb energy; the spherical-harmonic basis was truncated at  $l_{\max} = 4$  (i.e., including  $s$ ,  $p$ ,  $d$ ,  $f$ , and  $g$  symmetries); and the Green's functions were integrated using a complex-energy (semicircular) contour with 28 complex-energy points. The Brillouin zone integrations were performed via a Monkhorst-Pack [41]  $\Gamma$ -centered  $k$  mesh:  $24 \times 24 \times 16$  for a nonmagnetic (NM) state and  $32 \times 32 \times 24$  for FM and PM states. The PM state was described within the *disordered local moments* (DLM) approximation [42,43], with random orientations of local site-magnetic moments (i.e., zero magnetic short-range order) and zero average magnetization.

## IV. RESULTS AND DISCUSSION

The PXRD patterns recorded at room temperature confirm the formation of the  $\text{Ni}_2\text{In}$ -type hexagonal structure (space group  $P6_3/mmc$ ) in both samples. The fully refined PXRD pattern of sample 1 illustrated in Fig. 1 indicates a nearly single-phased  $\text{Pr}_2\text{In}$ . Given a rather high background, a small amount (less than 5 vol %, see below) of  $\text{Pr}_3\text{In}$  impurity phase may be present but cannot be conclusively detected in the material, even though a minor enhancement of the background, seen in the PXRD pattern and indicated by the arrow in Fig. 1, corresponds to the position of the strongest Bragg peak of  $\text{Pr}_3\text{In}$ . The PXRD pattern of sample 2 (not shown) is very similar but with a slightly higher amount of  $\text{Pr}_3\text{In}$  impurity. During grinding of the materials to prepare powders for x-ray measurements, it was noticed that the samples are quite soft and ductile, and as-ground powders exhibit a strong tendency toward clumping, which explains

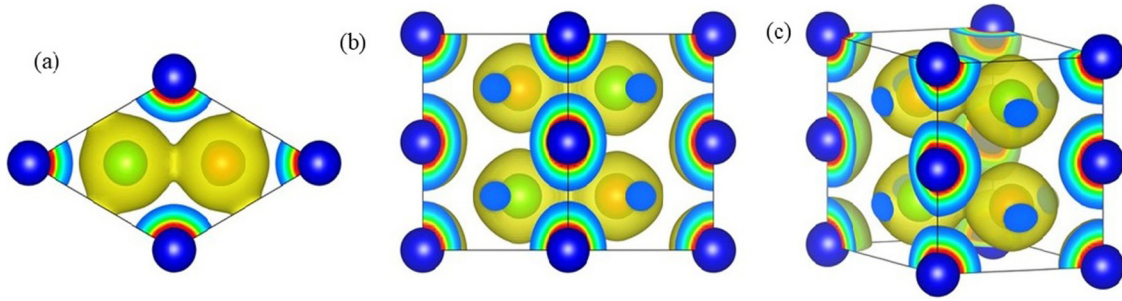


FIG. 2. Electron-density isosurfaces ( $0.02 e/\text{\AA}^3$ ) computed at  $c/a = 1.246$  for FM  $\text{Pr}_2\text{In}$  with  $\text{Ni}_2\text{In}$ -type hexagonal ( $P6_3/mmc$ ) structure in (a) [001], (b) [110] projections, and (c) perspective view.  $\text{Pr}_1$  ( $\text{Pr}_2$ ) is denoted with blue (green) spheres, and In are brown.

why the Bragg peaks are unusually broad in comparison with  $\text{Eu}_2\text{In}$  [8]. The stress introduced during the grinding could not be relieved by annealing due to high reactivity of the powders, contributing to the broadening of Bragg peaks and further enhancing the background. For sample 1, the refined lattice parameters are  $a = 5.539 \pm 0.006 \text{ \AA}$  and  $c = 6.902 \pm 0.01 \text{ \AA}$  ( $c/a = 1.246$ ), while the analysis of PXRD data for sample 2 (data not shown) leads to  $a = 5.539 \pm 0.002 \text{ \AA}$  and  $c = 6.895 \pm 0.003 \text{ \AA}$  ( $c/a = 1.245$ ). The lattice parameters of the two samples are indistinguishable within experimental errors, and they agree with previous reports [44,45], confirming that  $\text{Pr}_2\text{In}$  is a line compound with little, if any, homogeneity range. In sample 2,  $\text{Pr}_3\text{In}$  impurity was positively identified, and its concentration is 5 vol % according to the results of Rietveld refinement.

The electron density in real space was computed in VASP [37,38] with Perdew-Burke-Ernzerhof (PBE) exchange correlation [46] and the  $\Gamma$ -centered  $18^3 k$  mesh. VASP and MECCA results agree in FM and NM states (notably, DLM cannot be considered in VASP). The DFT-calculated electron density of  $\text{Pr}_2\text{In}$  is shown in Fig. 2, illustrating two Pr symmetry-distinctive sites and one In site. The atomic positions for  $\text{Pr}_1$ ,  $\text{Pr}_2$ , and In are, respectively,  $2a$  ( $x = y = z = 0$ ),  $2d$  ( $x = 1/3$ ,  $y = 2/3$ ,  $z = 3/4$ ), and  $2c$  ( $x = 1/3$ ,  $y = 2/3$ ,  $z = 1/4$ ). Figure 2 also shows a clear overlap between the electron density of In and  $\text{Pr}_2$ .

The temperature dependencies of magnetization of the two samples measured in a 1 kOe magnetic field indicate sharp, nearly discontinuous phase transitions between PM and FM states at  $T_C \cong 57 \text{ K}$  during both warming and cooling that occur without noticeable thermal hysteresis [Fig. 3(a)]. The difference in  $T_C$ 's of samples 1 and 2 is less than 2 K, suggesting that their actual stoichiometries are nearly the same and confirming a negligible homogeneity range [30]. The observed difference in  $T_C$  is most likely related to different concentrations of defects and interstitial impurities. Considering that the samples were cooled at different rates, a slightly higher  $T_C$  of sample 2 is expected due to larger grains compared to sample 1, as it is common for interstitial and other impurities to be rejected to grain boundaries when a material is allowed to crystallize slowly out of the melt [47,48]. The inverse magnetic susceptibility follows the Curie-Weiss law above  $T_C$  with an effective magnetic moment  $p_{\text{eff}} \cong 5.2 \mu_B/\text{f.u.}$  ( $\sim 3.67 \mu_B/\text{Pr}$ , as there are two independent Pr sites in  $\text{Pr}_2\text{In}$ ), close to the theoretical value of  $p_{\text{eff}} = g\sqrt{J(J+1)} = 3.58 \mu_B/\text{Pr}$ .

The transition remains sharp in magnetic fields up to 20 kOe, slowly shifting toward higher temperatures with the increasing magnetic field at the rate  $dT_C/dH \cong 0.2 \text{ K/kOe}$ , see Fig. 3(b). Both of the described features are typical signatures of an FOMPT. In addition to the nearly discontinuous transition at  $T_C$ , there exists a second, much broader and much weaker low-temperature anomaly in  $M(T)$  around 35 K [Figs. 3(a) and 3(b)], clearly observed in both samples. According to the PXRD study, the only known magnetic impurity phase in our samples is  $\text{Pr}_3\text{In}$ . For sample 1, the concentration of  $\text{Pr}_3\text{In}$  impurity is smaller than approximately 5 vol % of the same detected in sample 2. Earlier studies revealed that  $\text{Pr}_3\text{In}$  orders antiferromagnetically below 5 K [49,50], indicating that the anomaly at 35 K is intrinsic to the main  $\text{Pr}_2\text{In}$  phase. This anomaly is also detectable in specific heat data discussed later. This second anomaly is either a low-temperature spin reorientation transition or an electronic transition between two states with different Pr moments. In this context, it is worth mentioning that a similar low-temperature anomaly due to spin reorientation is also observed in  $\text{Nd}_2\text{In}$  [29,51], which shows a discontinuous transition at  $T_C$  as well [29].

Isothermal magnetization, measured as a function of the applied field after samples 1 and 2 were cooled to 5 K in zero magnetic field, is shown in Fig. 3(c). These measurements confirm the FM ground state with saturation magnetic moments of 1.61 and  $1.49 \mu_B/\text{Pr}$  for samples 1 and 2, respectively. Both values are smaller than expected from  $gJ = 3.2 \mu_B/\text{Pr}$ . Substantial crystalline electric field (CEF) interactions, reported to exist in all  $\text{R}_2\text{In}$  compounds, except when  $R = \text{Gd}$  [29], are most likely responsible for the reduction of the observed magnetic moment of  $\text{Pr}^{3+}$  due to splitting of the  $4f$  manifold. On the other hand, a noncollinear arrangement of Pr magnetic moments is also possible. The two samples, however, exhibit substantially different coercive fields and behaviors of  $M(H)$ . The coercivity of the polycrystalline material with randomly oriented fine grains (sample 1) is lower than that of randomly shaped, randomly oriented specimen composed of only a few large grains (sample 2), reflecting significant intrinsic magnetocrystalline anisotropy of the material. Further details of the anisotropic magnetic behaviors of the  $\text{Pr}_2\text{In}$  will be addressed in a followup study of an oriented single crystal. Sample 2 exhibits a slightly smaller saturation magnetic moment than sample 1 [Fig. 3(c)], which is related to the presence of a small amount of weakly magnetic  $\text{Pr}_3\text{In}$  [49,50].

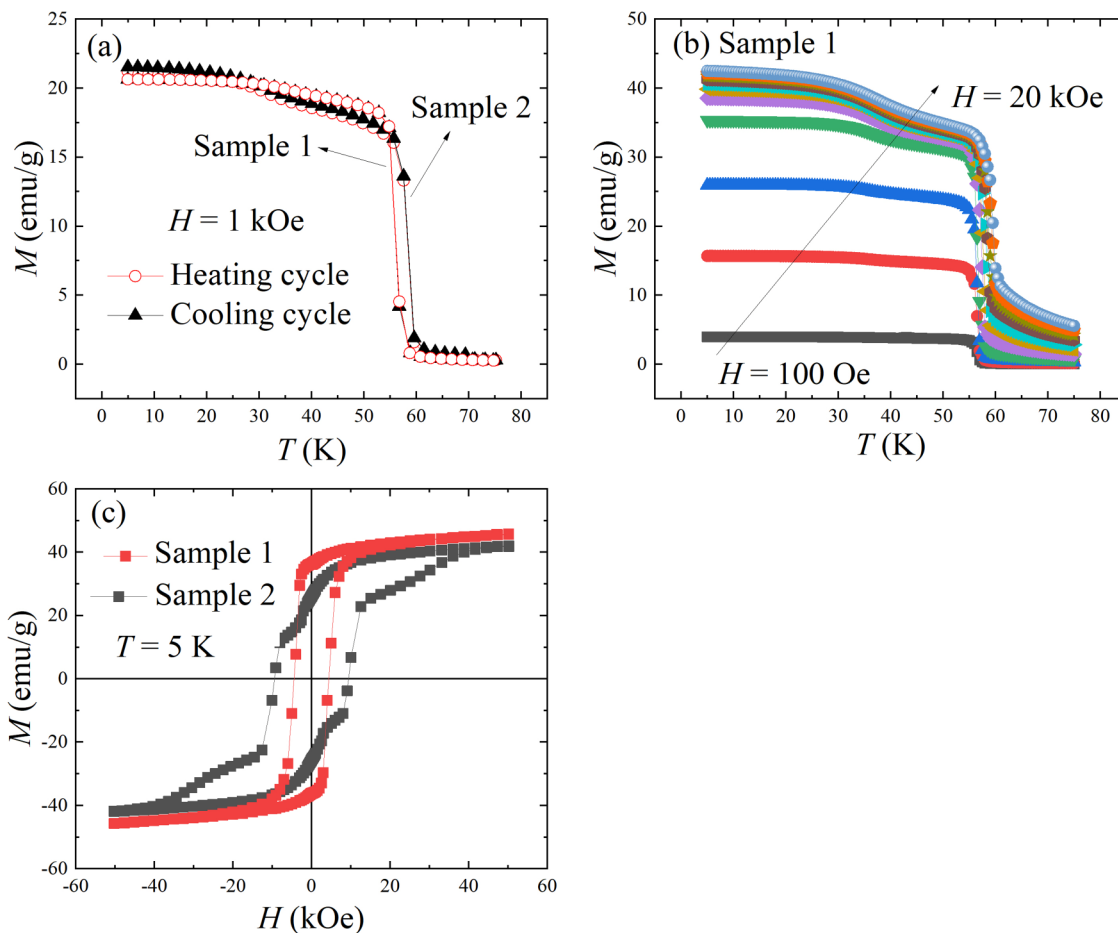


FIG. 3. (a) Magnetization vs temperature of samples 1 and 2 measured during cooling and heating in 1 kOe field; (b)  $M(T)$  data measured in different applied fields during heating (sample 1 only); and (c)  $M$  vs  $H$  of samples 1 and 2 recorded at 5 K.

The nature of a magnetic transition has a profound impact on the magnetocaloric effect exhibited by a material. The key parameter quantifying the magnetocaloric effect—magnetic-field-induced entropy change ( $\Delta S_M$ )—is expected to be large at FOMPT due to a sharp change of magnetization versus temperature. Regardless of the preparation method, both  $\text{Pr}_2\text{In}$  samples indeed show large  $\Delta S_M$  near  $T_C$  ( $\sim -15$  J/kg K for  $\Delta H = 20$  kOe), as illustrated in Fig. 4. The maximum values of  $\Delta S_M$  of  $\text{Pr}_2\text{In}$  are comparable to those observed in a number of magnetocaloric materials in the temperature range from 40 to 80 K and for the same magnetic field changes, for example,  $\text{HoCo}_2$  [52],  $\text{DyAl}_2$  [52],  $\text{GdNiAl}$  [52],  $\text{HoFeAl}$  [53],  $\text{TbN}$  [54],  $\text{HoZn}$  [55],  $\text{NdGa}$  [54],  $\text{TbCoAl}$  [54],  $\text{TbPtMg}$  [54],  $\text{Dy}_2\text{Co}_2\text{Al}$  [54],  $\text{Dy}_2\text{Cu}_2\text{In}$  [54], but are slightly lower than those observed in  $\text{Eu}_2\text{In}$  [8]. It is worth noting that changes in CEF-split  $4f$  manifolds that are known to occur in some Pr-based compounds at and below  $T_C$  [56] may also influence the magnitude of the magnetocaloric effect observed in  $\text{Pr}_2\text{In}$ .

Specific heat,  $C_P(T)$ , of sample 1 measured in 0 and 20 kOe applied fields is characterized by a sharp  $\Delta$  peak at  $T_C$  [Fig. 5(a)], consistent with FOMPT and in agreement with all of the data presented above, as well as with the earlier Mössbauer study [29]. A minor positive shift of the specific heat anomaly at 20 kOe compared with the same in zero field [inset, Fig. 5(a)] corroborates the weak magnetic field dependence of  $T_C$  determined from  $M(T)$  data. The broad  $M(T)$

anomaly at  $\sim 35$  K is also reflected by a broad maximum in  $C_P(T)$  at the same temperature. While calculating entropy

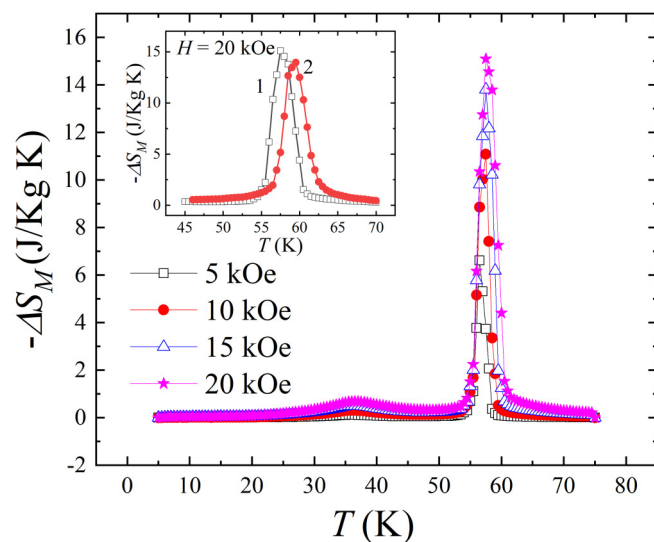


FIG. 4. Temperature dependence of the magnetic-field-induced entropy change,  $\Delta S_M$ , of sample 1 calculated from  $M(T)$  data measured in varying applied magnetic fields. Inset: Comparison of  $\Delta S_M$  of samples 1 and 2 for 20 kOe field change.

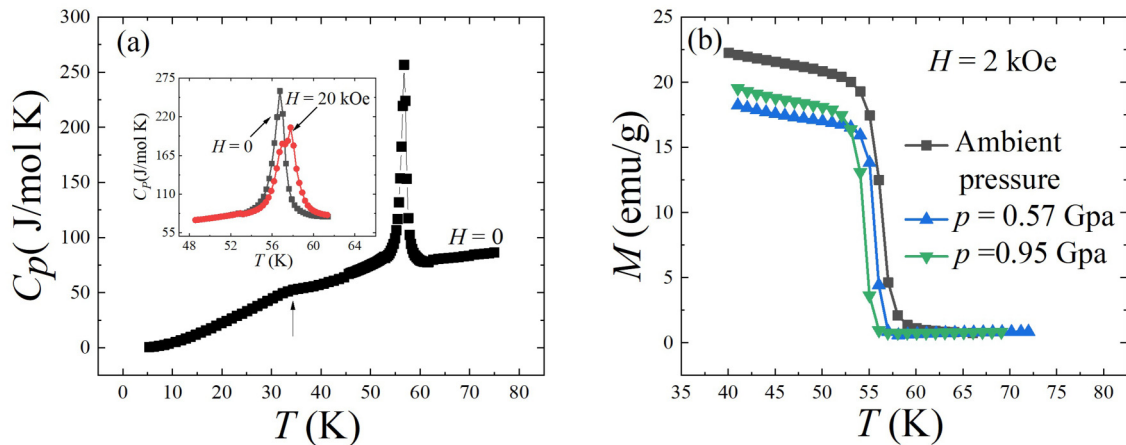


FIG. 5. (a)  $C_p$  vs  $T$  at zero magnetic field for sample 1. A weak anomaly is observed at low-temperature, as indicated by an arrow that corresponds to a broad anomaly observed in  $M(T)$ . Inset: Anomalous  $C_p$  in  $H = 0$  and 20 kOe near  $T_C$ . (b)  $M$  vs  $T$  measured in a 2 kOe field at different hydrostatic pressures.

change from  $C_p(T)$  measured at  $H = 0$  and 20 kOe, we found a smaller value ( $\sim -5$  J/kg K at the maximum) than  $\Delta S_M$  calculated from  $M(T)$  data. It is well known that acquiring accurate values of  $C_p$  at the first-order phase transition is difficult in some cases when using the relaxation method [8]. Therefore, the discrepancy in  $\Delta S_M$  calculated from specific heat and magnetization data is due to large errors in the values of anomalous specific heat at and in the immediate vicinity of the transition. Additional errors in specific heat are likely related to the loss of material due to sample reactivity (see Sec. IID, above). Therefore, the obtained heat-capacity data are only sufficient to qualitatively analyze the magnetothermal behavior of  $\text{Pr}_2\text{In}$ .

First-order phase transitions are commonly susceptible to hydrostatic pressure. In  $\text{Pr}_2\text{In}$ ,  $T_C$  shifts to lower temperatures with increasing pressure at the rate of  $dT_C/dp \cong -1.9$  K/GPa [Fig. 5(b)]. The value of  $dT_C/dp$  is nearly identical to that of  $\text{Eu}_2\text{In}$ , but the sign is opposite [8], and both are considerably weaker than in other FOMPTs [9,57]. From semi-quantitative specific heat data measured in zero field, we estimate the lower bound of entropy change at the transition as  $\delta S_T \sim 7.5$  J/mol K. Hence, the change in the lattice volume during the transition can be estimated from the Clausius-Clapeyron formalism [8] as  $\delta V = |\delta S_T(dT_C/dp)| \cong 0.01\%$ . The negative sign of  $dT_C/dp$  indicates that FM  $\text{Pr}_2\text{In}$  has a larger unit-cell volume than the high-temperature PM phase, which is opposite to that observed in  $\text{Eu}_2\text{In}$  [8]. Even though a nearly negligible phase volume change does not ensure equally negligible changes of two independent parameters of the hexagonal lattice, the former correlates with negligible hysteresis because strain due to lattice mismatch is among the dominant contributors to thermomagnetic hysteresis [18].

Narrow thermomagnetic hystereses have been reported for isosymmetric first-order transformations associated only with changes in phase volumes [8,15]. Considering negligible hysteresis observed in  $\text{Pr}_2\text{In}$ , one can assume that the symmetry and crystallography of this compound remain invariant across the transition, even though the latter requires experimental validation. This assumption finds further support in the fact that despite adopting a different type of crystal structure,

$\text{Eu}_2\text{In}$ , a closely related compound, also exhibits anhysteretic first-order phase transition without the change of its symmetry and with similarly small-phase-volume discontinuity [8]. It is, therefore, reasonable to postulate that  $\text{Pr}_2\text{In}$  retains its hexagonal  $\text{Ni}_2\text{In}$ -type structure at the ground state, and we use information derived from room-temperature PXRD data to perform first-principles computations.

The spin-resolved DOS of  $\text{Pr}_2\text{In}$  (see Fig. 6) is characterized by a sharp peak near  $E_F$  (mostly due to the majority spins of the  $4f$  states on both Pr sites). The large DOS near  $E_F$  is present in each state, i.e., FM and PM, and even the hypothetical NM. There also exists a large gradient in DOS near  $E_F$ , especially in the PM state. In this context, one may recall that a large DOS near  $E_F$  is also present in  $\text{Eu}_2\text{In}$  [8], in which a FOMPT occurs. Thus, by comparing DFT results of  $\text{Pr}_2\text{In}$  with previously studied  $\text{Eu}_2\text{In}$  [8], it is concluded that a large DOS along with a large gradient at  $E_F$  is a generic feature for these chemically related but structurally different materials. Such a peculiar DOS behavior is responsible for creating the electronic instability required for the FOMPT.

As shown in the electron density (Fig. 2), there is a clear overlap of the occupied electronic orbitals of In and Pr, which is larger for  $\text{Pr}_2$  and smaller for  $\text{Pr}_1$ . However, an overlap in real space is a necessary but not sufficient condition for hybridization of In  $5p$  and Pr  $4f$  electrons. At  $E_F$  in the PM state, all In states contribute 3.3 states/Ry/spin for each spin, while the In  $5p$  states contribute only 1.4 states/Ry/spin, small compared to the majority-spin contributions of 221 states/Ry/spin from all  $\text{Pr}_1$  (including 210 from  $4f$  states) and 239 states/Ry/spin from all  $\text{Pr}_2$  states (including 231 from  $4f$ ). The minority spin at  $E_F$  contributes 12.6 states/Ry/spin from  $\text{Pr}_1$  and 8.0 states/Ry/spin from  $\text{Pr}_2$  states, including 3.5 and 2.6 states/Ry/spin from  $\text{Pr}_1$  and  $\text{Pr}_2$   $4f$  states, respectively [Fig. 6(b)]. Thus the hybridization of Pr  $5d$  states with In  $5p$  is insignificant at  $E_F$  in  $\text{Pr}_2\text{In}$  [Fig. 6(b)] compared to the case in  $\text{Eu}_2\text{In}$ , where hybridization between Eu and In orbitals near  $E_F$  was reported [8].

Figures 7(a) and 7(b), respectively, present the variation of computed site-magnetic moments ( $m_a$ ) and DFT

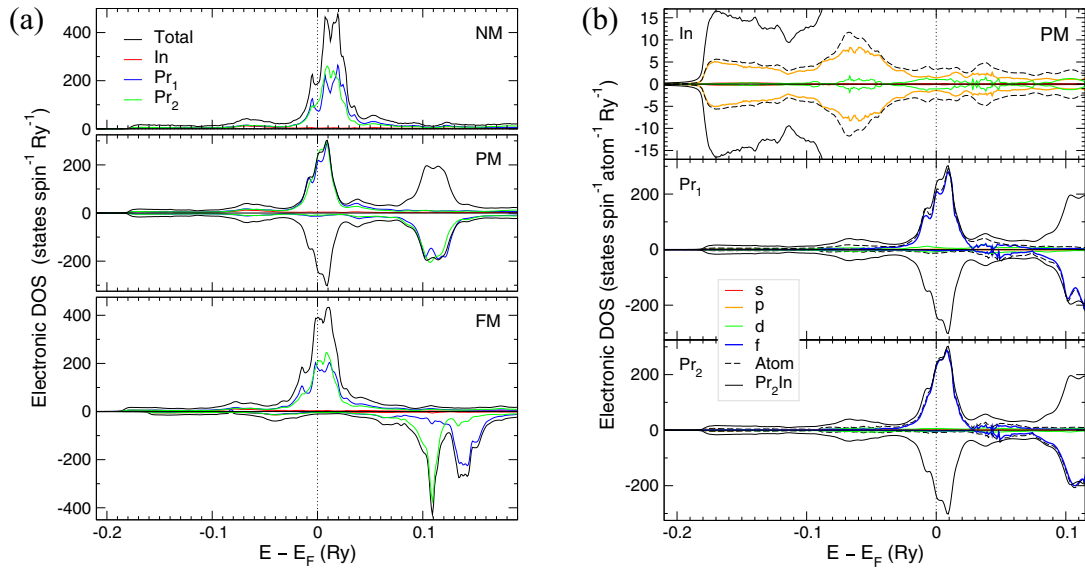


FIG. 6. (a) Total (per Pr<sub>2</sub>In f.u.) and site-projected electronic DOS in NM, PM, and FM states vs energy  $E$  relative to the Fermi energy,  $E_F$ , calculated at  $c/a = 1.246$ . Indium contribution to DOS near  $E_F$  is small (e.g., 3.3 states/Ry/spin for each spin at  $E_F$  in the PM state). (b) Atomic orbital- and spin-projected DOS in PM state.

energy ( $E$ ) with lattice parameter  $a$  (and  $c/a$  fixed at the experimentally measured ratio) in different magnetic states. Here,  $E$  vs  $a$  is fitted according to the Birch-Murnaghan equation of state [58,59]. The calculated amplitudes of the Pr<sub>1</sub> and Pr<sub>2</sub> site-magnetic moments in the FM state differ [Fig. 7(a)] from those in the PM state. A discontinuous change of the electronic state (and hence magnetic moments) between FM and PM states near the equilibrium lattice constant [Fig. 7(a)] is a feature of a first-order transition. In addition, the calculated equilibrium lattice constants in FM and PM states are within 0.1% [Fig. 7(b)]. This agrees with the negligible phase volume change during the transition estimated using the Clausius-Clapeyron equation,

which leads to a small thermomagnetic hysteresis in the material.

Electronic enthalpy depends on the total electronic DOS at  $E_F$ , while magnetic entropy of the PM state monotonically increases with the atomic magnetic moments [17]. The thermodynamic estimators described earlier [17] point to a large entropy change at the FOMPT in Pr<sub>2</sub>In, even though CEF interactions may lower  $\Delta S_M$  [56]. Indeed, we observe quite a large magnetic entropy change in this compound (Fig. 4). Therefore, our theoretical results agree quite well with our experimental observations.

Experimentally, FOMPT in Pr<sub>2</sub>In is reminiscent of that observed in Eu<sub>2</sub>In. However, the two are different not only

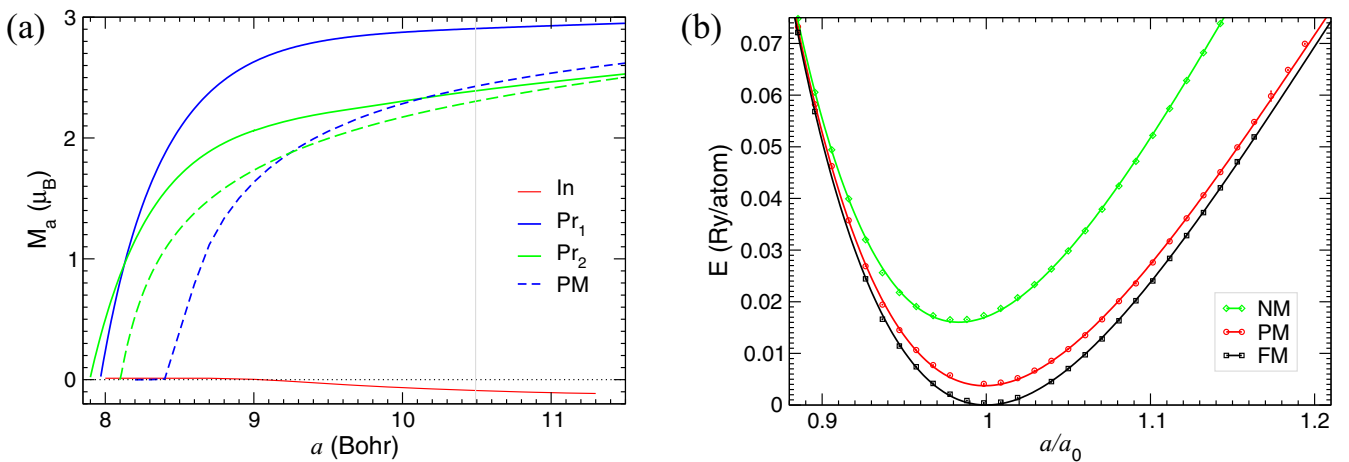


FIG. 7. (a) Computed site-magnetic moments  $m_a$  vs  $a$  at fixed  $c/a$  in FM and PM states. Indium moment is  $0 \mu_B$  in PM state. The lattice constant of Pr<sub>2</sub>In (vertical dotted line) measured at room temperature. (b) DFT energy  $E$  (mRy/atom, relative to FM state) vs  $a$  at fixed  $c/a$  in the NM, PM, and FM states. Points (lines) are DFT (fit by Birch-Murnaghan [58,59] equation of state). Equilibrium lattice constant ( $a_0$ ) changes by less than 0.1% at FM-PM transition.

in terms of their room-temperature crystal structures but also in terms of the mechanisms of magnetic-exchange interactions. In the PM state, Pr<sub>2</sub>In adopts the hexagonal Ni<sub>2</sub>In-type structure, in contrast to the orthorhombic Co<sub>2</sub>Si-type structure of Eu<sub>2</sub>In. The indirect  $4f-4f$  interactions in Pr<sub>2</sub>In responsible for the long-range magnetic ordering are conventional. They are mediated by Pr  $4f-Pr 5d$  polarization and  $5d-5d$  exchange interaction between neighboring Pr atoms [24,25]; hence the role of In in developing FM order is limited to the stabilization of the hexagonal lattice with interatomic distances supporting positive magnetic-exchange energy. This view is also reflected in our DFT results that show a negligible contribution of In in the total DOS near  $E_F$  (Fig. 6). For the case of Eu<sub>2</sub>In, the Eu  $5d$  shell is empty as Eu is in the Eu<sup>2+</sup> state. However, the unoccupied Eu  $5d$  states gain electrons from hybridization with the occupied In  $5p$  states, enabling Eu  $4f-5d$  exchange. Therefore, In plays a critical role in developing ferromagnetism of Eu<sub>2</sub>In, in addition to stabilizing a specific crystal lattice of the latter [8]. Hence, the magnetic-exchange interactions are mechanistically different in these two compounds. Despite that fact, substantially enhanced DOS near the Fermi energy found in both Pr<sub>2</sub>In and Eu<sub>2</sub>In underpins both the first-order magnetic transitions and large magnetocaloric effects observed in these two materials. Furthermore, nearly negligible thermal hysteresis observed in these crystallographically different intermetallic compounds is related to very minor volume changes across FOMPTs in both materials.

## V. CONCLUSIONS

We observed a rare first-order magnetic transition with a miniscule thermomagnetic hysteresis in Pr<sub>2</sub>In. The material exhibits a large magnetic-field-induced entropy change,  $-15$  J/kg K for  $\Delta H = 20$  kOe, near its  $T_C = 57$  K. Both the magnetization and heat-capacity measurements confirm the first-order nature of the transition. A second, weaker magnetic transition is visible at 35 K. Our theory and calculations explain the underlying science of the first-order magnetic transition in terms of a specific electronic structure with a large electronic spin DOS near  $E_F$  along with a large gradient in the DOS. The pressure-dependent magnetization yields  $dT_C/dp \cong -1.9$  K/GPa, which is considerably smaller compared to the cases of commonly observed FOMPTs. Both theoretical and experimental results point to the small volume change at the transition as the likely reason for the observed negligible thermomagnetic hysteresis.

## ACKNOWLEDGMENTS

This work was performed at Ames Laboratory of the US Department of Energy (DOE) and was supported by the Division of Materials Science and Engineering, Basic Energy Sciences, Office of Science of the US DOE. Ames Laboratory is operated for the US DOE by Iowa State University of Science and Technology under Contract No. DE-AC02-07CH11358. The authors are thankful to P. O. Ribeiro and B. P. Alho for fruitful discussions.

- 
- [1] S. B. Roy, First-order magneto-structural phase transition and associated multi-functional properties in magnetic solids, *J. Phys.: Condens. Matter* **25**, 183201 (2013).
- [2] N. T. Trung, L. Zhang, L. Caron, K. H. J. Buschow, and E. Bruck, Giant magnetocaloric effects by tailoring the phase transitions, *Appl. Phys. Lett.* **96**, 172504 (2010).
- [3] J. Liu, Y. Gong, G. Xu, G. Peng, I. A. Shah, N. U. Hassan, and F. Xu, Realization of magnetostructural coupling by modifying structural transitions in MnNiSi-CoNiGe system with a wide Curie-temperature window, *Sci. Rep.* **6**, 23386 (2016).
- [4] Z. Wei, E. Liu, Y. Li, G. Xu, X. Zhang, G. Liu, X. Xi, H. Zhang, W. Wang, G. Wu, and X. Zhang, Unprecedentedly wide Curie-temperature windows as phase-transition design platform for tunable magneto-multifunctional materials, *Adv. Electron. Mater.* **1**, 1500076 (2015).
- [5] O. Gutfleisch, T. Gottschall, M. Fries, D. Benke, I. Radulov, K. P. Skokov, H. Wende, M. Gruner, M. Acet, P. Entel, and M. Farle, Mastering hysteresis in magnetocaloric materials, *Philos. Trans. R. Soc., A* **374**, 20150308 (2016).
- [6] K. A. Gschneidner, Jr. and V. K. Pecharsky, Magnetocaloric materials, *Annu. Rev. Mater. Sci.* **30**, 387 (2000).
- [7] V. K. Pecharsky and K. A. Gschneidner, Jr., Giant Magnetocaloric Effect in Gd<sub>5</sub>(Si<sub>2</sub>Ge<sub>2</sub>), *Phys. Rev. Lett.* **78**, 4494 (1997).
- [8] F. Guillou, A. K. Pathak, D. Paudyal, Y. Mudryk, F. Wilhelm, A. Rogalev, and V. K. Pecharsky, Non-hysteretic first-order phase transition with large latent heat and giant low-field magnetocaloric effect, *Nat. Commun.* **9**, 2925 (2018).
- [9] A. Biswas, A. K. Pathak, N. A. Zarkovich, X. Liu, Y. Mudryk, V. Balema, D. D. Johnson, and V. K. Pecharsky, Designed materials with the giant magnetocaloric effect near room temperature, *Acta Mater.* **180**, 341 (2019).
- [10] H. N. Bez, A. K. Pathak, A. Biswas, N. Zarkevich, V. Balema, Y. Mudryk, D. D. Johnson, and V. K. Pecharsky, Giant enhancement of the magnetocaloric response in Ni-Co-Mn-Ti by rapid solidification, *Acta Mater.* **173**, 225 (2019).
- [11] X. M. Sun, D. Y. Cong, Z. Li, Y. L. Zhang, Z. Chen, Y. Ren, K. D. Liss, Z. Y. Ma, R. G. Li, Y. H. Qu, Z. Yang, L. Wang, and Y. D. Wang, Manipulation of magnetostructural transition and realization of prominent multifunctional magneto-responsive properties in NiCoMnIn alloys, *Phys. Rev. Mater.* **3**, 034404 (2019).
- [12] L. H. Lewis, C. H. Marrows, and S. Langridge, Coupled magnetic, structural, and electronic phase transitions in FeRh, *J. Phys. D: Appl. Phys.* **49**, 323002 (2016).
- [13] A. Biswas, Y. Mudryk, A. K. Pathak, L. Zhou, and V. K. Pecharsky, Managing hysteresis of Gd<sub>5</sub>Si<sub>2</sub>Ge<sub>2</sub> by magnetic field cycling, *J. Appl. Phys.* **126**, 243902 (2019).
- [14] F. X. Hu, B. Shen, J. Sun, and Z. Cheng, Influence of negative lattice expansion and metamagnetic transition on magnetic entropy change in the compound LaFe<sub>11.4</sub>Si<sub>1.6</sub>, *Appl. Phys. Lett.* **78**, 3675 (2001).
- [15] A. Fujita, S. Fujieda, Y. Hasegawa, and K. Fukamichi, Itinerant-electron metamagnetic transition and large magnetocaloric effects in La(Fe<sub>x</sub>Si<sub>1-x</sub>)<sub>13</sub> compounds and their hydrides, *Phys. Rev. B* **67**, 104416 (2003).



- [16] N. A. Zarkevich, D. D. Johnson, and V. K. Pecharsky, High-throughput search for caloric materials: The CaloriCool approach, *J. Phys. D: Appl. Phys.* **51**, 024002 (2018).
- [17] N. A. Zarkevich and D. D. Johnson, Reliable thermodynamic estimators for screening caloric materials, *J. Alloys Compd.* **802**, 712 (2019).
- [18] J. Cui, Y. S. Chu, O. Famodu, Y. Furuya, J. H. Simpers, R. D. James, A. Ludwig, S. Thienhaus, M. Wuttig, Z. Zhang, and I. Takeuchi, Combinatorial search of thermoelastic shape-memory alloys with extremely small hysteresis width, *Nat. Mater.* **5**, 286 (2006).
- [19] F. Guillou, G. Porcari, H. Yibole, N. van Dijk, and E. Bruck, Taming the first-order transition in giant magnetocaloric materials, *Adv. Mater.* **26**, 2671 (2014).
- [20] E. Bruck, H. Yibole, and L. A. Zhang, A universal metric for ferroic energy materials, *Philos. Trans. R. Soc., A* **374**, 20150303 (2016).
- [21] J. Lyubina, Magnetocaloric materials for energy efficient cooling, *J. Phys. D: Appl. Phys.* **50**, 053002 (2017).
- [22] J. Jensen and A. R. Mackintosh, Rare earth magnetism, *The International Series of Monographs on Physics*, edited by J. Birman, S. F. Edwards, C. H. Llewellyn, and S. M. Rees (Clarendon Press, Oxford, 1991).
- [23] T. Kasuya, A theory of metallic ferro- and antiferromagnetism on Zener's model, *Prog. Theor. Phys.* **16**, 45 (1956).
- [24] I. A. Campbell, Indirect exchange for rare earths in metals, *J. Phys. F: Met. Phys.* **2**, L47 (1972).
- [25] L. Petit, Z. Szotek, D. Paudyal, A. Biswas, Y. Mudryk, V. K. Pecharsky, and J. B. Staunton, Magnetic structure of selected Gd intermetallic alloys from first principles, *Phys. Rev. B* **101**, 014409 (2020).
- [26] S. Khmelevskiy and P. Mohn, The order of the magnetic phase transitions in  $\text{RCO}_2$  ( $R = \text{rare earth}$ ) intermetallic compounds, *J. Phys.: Condens. Matter* **12**, 9453 (2000).
- [27] Y. Mudryk, D. Paudyal, A. K. Pathak, V. K. Pecharsky, and K. A. Gschneidner, Jr., Balancing structural distortions *via* competing 4f and itinerant interactions: A case of polymorphism in magnetocaloric  $\text{HoCo}_2$ , *J. Mater. Chem. C* **4**, 4521 (2016).
- [28] V. K. Pecharsky, A. P. Holm, K. A. Gschneidner, and R. Rink, Massive Magnetic-Field-Induced Structural Transformation in  $\text{Gd}_5\text{Ge}_4$  and the Nature of the Giant Magnetocaloric Effect, *Phys. Rev. Lett.* **91**, 197204 (2003).
- [29] M. Forker, R. Mubeler, S. C. Bedi, M. Olzon-Dionysio, and S. Dionysio de Souza, Magnetic and electric hyperfine interactions in the rare-earth indium compounds  $\text{R}_2\text{In}$  studied by  $^{111}\text{Cd}$  perturbed angular correlations, *Phys. Rev. B* **71**, 094404 (2005).
- [30] PAULING FILE, in *Inorganic Solid Phases*, edited by P. Villars, Springer Materials (online database) (Springer, Heidelberg); Springer Materials, In-Pr Binary Phase Diagram 65–100 at % Pr, [https://materials.springer.com/isp/phase-diagram/docs/c\\_0903174](https://materials.springer.com/isp/phase-diagram/docs/c_0903174).
- [31] J. Rodriguez-Carvajal, Recent advances in magnetic structure determination by neutron powder diffraction, *Physica B* **192**, 55 (1993).
- [32] H. Neves Bez, H. Yibole, A. Pathak, Y. Mudryk, and V. K. Pecharsky, Best practices in evaluation of the magnetocaloric effect from bulk magnetization measurements, *J. Magn. Magn. Mater.* **458**, 301 (2018).
- [33] L. Tocado, E. Palacios, and R. Burriel, Entropy determinations and magnetocaloric parameters in systems with first-order transitions: Study of  $\text{MnAs}$ , *J. Appl. Phys.* **105**, 093918 (2009).
- [34] J. Korringa, On the calculation of the energy of a Bloch wave in a metal, *Physica* **13**, 392 (1947).
- [35] W. Kohn and N. Rostoker, Solution of the Schrödinger equation in periodic lattices with an application to metallic lithium, *Phys. Rev.* **94**, 1111 (1954).
- [36] D. D. Johnson, A. V. Smirnov, and S. N. Khan, MECCA: multiple-scattering electronic-structure calculations for complex alloys (KKR-CPA Program, ver. 2.0), Iowa State University and Ames Laboratory, 2015.
- [37] A. Alam, S. N. Khan, A. V. Smirnov, D. M. Nicholson, and D. D. Johnson, Green's function multiple-scattering theory with a truncated basis set: An augmented-KKR formalism, *Phys. Rev. B* **90**, 205102 (2014).
- [38] G. Kresse and J. Hafner, *Ab initio* molecular dynamics for liquid metals, *Phys. Rev. B* **47**, 558(R) (1993).
- [39] G. Kresse and J. Hafner, *Ab initio* molecular-dynamics simulation of the liquid-metal–amorphous–semiconductor transition in germanium, *Phys. Rev. B* **49**, 14251 (1994).
- [40] J. P. Perdew, A. Ruzsinszky, G. Csonka, I. Abor, A. O. Vydrov, E. G. Scuseria, A. L. Constantin, X. Zhou, and K. Burke, Restoring the Density-Gradient Expansion for Exchange in Solids and Surfaces, *Phys. Rev. Lett.* **100**, 136406 (2008).
- [41] H. J. Monkhorst and J. D. Pack, Special points for Brillouin-zone integrations, *Phys. Rev. B* **13**, 5188 (1976).
- [42] B. L. Gyorffy, A. J. Pindor, G. M. Stocks, J. Staunton, and H. Winter, A first-principles theory of ferromagnetic phase transitions in metals, *J. Phys. F: Met. Phys.* **15**, 1337 (1985).
- [43] D. D. Johnson, D. M. Nicholson, F. J. Pinski, B. L. Gyorffy, and G. M. Stocks, Density-Functional Theory for Random Alloys: Total Energy within the Coherent-Potential Approximation, *Phys. Rev. Lett.* **56**, 2088 (1986).
- [44] A. Palenzona, The crystal structure and lattice constants of  $\text{R.E.}_2\text{In}$  and some  $\text{R.E.}_5\text{In}_3$  compounds, *J. Less-Common Met.* **16**, 379 (1968).
- [45] E. Franceschi, On the crystal structure of  $\text{R.E.}_5\text{In}_3$ , *J. Less-Common Met.* **37**, 157 (1974).
- [46] J. P. Perdew, K. Burke, and M. Ernzerhof, Generalized Gradient Approximation Made Simple, *Phys. Rev. Lett.* **77**, 3865 (1996).
- [47] D. Fort, V. K. Pecharsky, and K. A. Gschneidner, Jr., Solid state electrotransport purification of dysprosium, *J. Alloys Compd.* **226**, 190 (1995).
- [48] V. K. Pecharsky, K. A. Gschneidner, and D. Fort, Superheating and other unusual observations regarding the first order phase transition in Dy, *Scr. Mater.* **35**, 843 (1996).
- [49] R. D. Hutchens, W. E. Wallace, and N. G. Nereson, Magnetic properties of  $\text{Ln}_3\text{In}$  intermetallic compounds, *J. Solid State Chem.* **9**, 152 (1974).
- [50] A. D. Christianson, J. M. Lawrence, K. C. Littrell, E. A. Goremychkin, A. I. Kolesnikov, J. D. Thompson, and J. L. Sarrao, Crystal field excitations in the singlet ground state compound  $\text{Pr}_3\text{In}$ , *J. Appl. Phys.* **101**, 09D505 (2007).
- [51] N. N. Delyagin, G. T. Mujiri, and V. I. Nesterov, Exchange and hyperfine interactions in the magnetic intermetallic compounds  $\text{R}_2\text{In}$ , *Sov. Phys. JETP* **69**, 1070 (1989).
- [52] A. M. Tishin and Y. I. Spichkin, *The Magnetocaloric Effect and Its Applications* (IOP Publishing, Bristol, 2003).
- [53] Y. Zhang, G. Wilde, X. Li, Z. Ren, and L. Li, Magnetism and magnetocaloric effect in the ternary equiatomic

- REFeAl (RE = Er and Ho) compounds, [Intermetallics](#) **65**, 61 (2015).
- [54] T. A. Yamamoto, T. Nakagawa, K. Sako, T. Arakawa, and H. Nitani, Magnetocaloric effect of rare earth mono-nitrides, TbN and HoN, [J. Alloys Compd.](#) **376**, 17 (2004).
- [55] L. Li and M. Yan, Recent progress in exploring the rare earth based intermetallic compounds for cryogenic refrigeration, [J. Alloys Compd.](#) **823**, 153810 (2020).
- [56] P. J. von Ranke, N. A. Oliveira, C. Mello, D. C. Garcia, V. S. R. de Sousa, V. A. de Souza, A. Caldas, and I. G. de Oliveira, The influence of quadrupolar interaction on the magnetocaloric effect in PrMg, [J. Alloys Compd.](#) **440**, 46 (2007).
- [57] S. Yuce, M. Barrio, B. Emre, E. Stern-Taulats, A. Planes, J.-L. Tamarit, Y. Mudryk, K. A. Gschneidner, and V. K. Pecharsky, Barocaloric effect in the magnetocaloric prototype Gd<sub>5</sub>Si<sub>2</sub>Ge<sub>2</sub>, [Appl. Phys. Lett.](#) **101**, 071906 (2012).
- [58] F. Birch, Finite elastic strain of cubic crystals, [Phys. Rev.](#) **71**, 809 (1947).
- [59] F. D. Murnaghan, The compressibility of media under extreme pressures, [Proc. Natl. Acad. Sci. USA](#) **30**, 244 (1944).